Pergamon

Int. J. Multiphase Flow Vol. 22, No. 2, pp. 379–402, 1996

0301-9322(95)00072-0
0301-9322/96 $15.00 + 0.00

THE MULTIPHASE PARTICLE-IN-CELL (MP-PIC) METHOD FOR DENSE PARTICULATE FLOWS

M. J. ANDREWS[1] and P. J. O'ROURKE[2]

[1]Department of Mechanical Engineering, Texas A&M University, College Station, TX 77843-3123, U.S.A.
[2]Theoretical Division, Los Alamos National Laboratory, Los Alamos, NM 87545, U.S.A.

(Received 15 December 1994; in revised form 5 October 1995)

Abstract—A multiphase particle-in-cell (MP-PIC) method has been developed. This numerical technique draws upon the best of Eulerian/Eulerian continuum models and Eulerian/Lagrangian discrete models. The MP-PIC method uses an accurate mapping from Lagrangian particles to and from a computational grid. While on the grid, continuum derivative terms that treat the particle phase as a fluid are readily evaluated and then mapped back to individual particles. The result of this procedure is a computational technique for multiphase flows that can handle particulate loading ranging from dense to dilute, a distribution of particle sizes and a range of particle materials. The dense particulate model represents separated flows of particles and includes drag exerted by a gas phase, inter-particle stresses, particle viscous stresses and gas pressure gradients. Six problems are presented to demonstrate the MP-PIC method. This MP-PIC method has important applications in fluidized beds (combustion, catalytic cracking), sedimentation, separation and many other granular flows.

Key Words: MP-PIC, sedimentation, separation, fluidized beds, CFD, one-dimensional, comprehensive multiphase flow

1. INTRODUCTION

The modeling of dense particulate flows in fluidized beds and elsewhere has recently received considerable attention because of questions of stability and formulation of well-posed governing equations (Batchelor 1988; Harris & Crighton 1994). Such particulate flows are generally represented with a separated-flow model where the different phases have separate, but not necessarily the same, velocities. Each phase exerts an influence on the other phases and itself through terms such as drag, mean gas pressure gradient, inter-particle stresses and particle viscous stresses (Batchelor 1988). These latter two terms make the model equations well-posed (Lyczkowski 1978; Gidaspow 1986; Harris & Crighton 1994) and are summarily included in this work.

Mathematical models of separated particulate multiphase flow have either used Eulerian continuum governing equations for all phases (Gidaspow 1986; Batchelor 1988) or a Lagrangian description for the particulate phase, and an Eulerian continuum description for the gas phase (Williams 1985). Kuo (1986) and Gidaspow (1994) give a thorough discussion of two-phase flow models. Continuum models are more common for dense particulate flows and intuitively make sense, for common experience suggests that fluidized, dense-packed granules flow like a fluid. These continuum models readily allow the modeling of particle–particle stresses and particle–viscous stresses using spatial gradients of phase volume fractions and velocities (Batchelor 1988; Gidaspow *et al.* 1994). However, the introduction of a particle size distribution greatly complicates the formulation and requires the introduction of equations to follow the movement of different particle sizes (Risk 1993). Thus, many separate continuity and momentum equations are required (Risk 1993; Gidaspow *et al.* 1994) to accurately represent separated flows with different particle sizes.

An alternative formulation is to use a Lagrangian description for the particle phase and an Eulerian one for the underlying continuous gas phase. Trajectory and momentum equations for individual particles are implicitly fully coupled with the gas phase. In such a Lagrangian model, each particle can have different characteristics (size, density, shape, velocity), and the result is an truly multiphase model. If the particles have a distribution of velocities $\mathbf{v}$ and masses m, the Lagrangian method seeks to solve an equation for the solid phase distribution function $f(\mathbf{x}, \mathbf{v}, m, t)$ and has at its root a stochastic formulation closely related to the recent development of a kinetic

theory for granular flows (Jenkins & Savage 1983; Lun *et al.* 1984; Gidaspow 1994). Such a formulation for liquid sprays was given by O'Rourke (1981), where the particle equations were solved with a stochastic particle method that included the effects of droplet collisions. However, the particle collision frequency is high when the particulate volume fractions are above 5% and cannot be realistically resolved within a Lagrangian collision calculation. Typical applications of the stochastic particle method are dispersed phase flows such as sprays (Andrews 1989, 1991).

Here we present a numerical simulation procedure for multiphase flows that consistently blends discrete Lagrangian and continuum Eulerian methods. For single-phase flows the particle-in-cell technique (Harlow 1964) has recently undergone several significant improvements (O'Rourke *et al.* 1993) and provides a natural structure for multiphase simulations. The consequence of our efforts is a multiphase PIC method, called MP-PIC, which provides an accurate and consistent representation of both discrete and continuum multiphase models. This paper describes the formulation of the MP-PIC equations and a one-dimensional implementation to demonstrate the MP-PIC method. Six non-trivial multiphase test problems are solved with the most complex being a sedimentation and separation of a mixture of particles with three different sizes. When possible, the computational solutions are compared with analytical ones to establish the accuracy of the numerical formulation.

The paper closes with our conclusions from the work presented and references.

2. THE EQUATIONS OF MOTION

We first give the equations solved by the MP-PIC method. The formulation is asymmetric in the sense that, while mass and momentum equations are solved for the continuous phase, for the particle phase a Liouville equation is solved for the distribution function of particle positions, velocities and sizes. The MP-PIC equations contain terms that are either not contained in, or whose form is altered from terms contained in, the usual continuum and particle/fluid formulations of multiphase flow. To motivate these terms we indicate later in this section how mass and momentum equations for the particle phase can be derived by taking moments of the Liouville equation. Our equations include the essential fetures of all dense particulate flows, including the displacement of gas volume by the particle phase and the strong collisional forces amongst the particles. To model the average collisional force we have followed common practice (Gidaspow 1986; Harris & Crighton 1994) by using an isotropic solids stress that depends on the particle volume fraction.

To focus on the new numerical methodology, we have simplified the most general multiphase problem by making several assumptions. First, we neglect fluctuating forces on the particles caused by fluctuating gas velocities and by particle collisions. The former effect has been modeled in particle/fluid methods (Andrews & Bracco 1989; O'Rourke 1989) by including in the particle drag term a fluctuating gas velocity that is stochastically chosen using the local gas turbulent kinetic energy and turbulence dissipation rate. We will use this same approach in future work. Second, we are neglecting off-diagonal elements of the solids stress tensor. Third, we neglect the mean force on particles of a given size due to collisions with particles of other sizes. This so-called interlocking effect, which may be important only at very high particle loadings (Davies 1968), will also be the subject of future research. Additional simplifying assumptions we have made are that the continuous phase is a gas, the gas is perfect with constant entropy, the gas is inviscid (viscosity is significant on the scale of the particles, where it enters the particle drag formula), the particle density is constant and the same for each particle, and there is no mass exchange between the phases.

The only test case in this paper which we compare with experimental data is the last, which involves the sedimentation of a mixture of three particle sizes, and some may question the neglect of fluctuating particle forces in this problem. Such forces broaden and skew the particle velocity distribution and therefore enhance the particle kinematic stress that is implicit in our equations. (See [12] below.) It is important to include this effect in problems with gradients in the mean particle velocity. In the test case, however, there are only regions of nearly constant mean particle velocity separated by kinematic shocks (Kynch 1952). The fluctuating forces are expected to result in some broadening of the shocks but otherwise not effect the result.

The use of an adiabatic gas equation of state may also bother some. We certainly do not defend its use in general, but we maintain that it is appropriate for the problems of this paper. The implicit numerical formulation we will give later is such that one can efficiently calculate flows with very small Mach numbers. When Mach numbers are very small, sound waves are numerically damped; and the numerical solutions obtained are those for incompressible flow, in which the equation of state is irrelevant. This is the case for the four test cases we present later involving sedimentation, in which we are simulating incompressible, isothermal systems. Only one test case involves compressibility effects in the gas, and this is the first one, in which we calculate the sound speed in a multiphase mixture for purposes of comparing with an analytic solution.

The mass and momentum equations for the gas phase are (Wallis 1969; Batchelor 1988; Gidaspow 1994):

$$\frac{\partial(\epsilon\rho_G)}{\partial t} + \nabla_x\cdot(\epsilon\rho_G\mathbf{u}_G) = 0 \qquad [1]$$

and

$$\frac{\partial(\epsilon\rho_G\mathbf{u}_G)}{\partial t} + \nabla_x\cdot(\epsilon\rho_G\mathbf{u}_G\mathbf{u}_G) + \nabla_x p = -\mathbf{F} + \epsilon\rho_G\mathbf{g}, \qquad [2]$$

where ϵ is the gas volume fraction (or void fraction), ρ_G is the gas density (gas mass per unit volume occupied by the gas), $\mathbf{u}_G$ is the gas velocity, p is the gas pressure, $\mathbf{g}$ the acceleration due to gravity and $\mathbf{F}$ is the rate of momentum exchange per unit volume from the gas to the particle phase. The gas pressure and density are related by

$$\frac{p}{\rho_G^{\gamma}} = \text{constant}. \qquad [3]$$

We give the detailed expression for $\mathbf{F}$ later after introducing the particle distribution function.

The evolution of the particle phase is governed by a Liouville equation for the particle distribution function $f(\mathbf{x}, \mathbf{v}, m, t)$, where $\mathbf{x}$ is the particle position, $\mathbf{v}$ is the particle velocity and m is the particle mass:

$$\frac{\partial f}{\partial t} + \nabla_x\cdot(f\mathbf{v}) + \nabla_v\cdot(f\mathbf{A}) = 0. \qquad [4]$$

In this equation $\mathbf{A} = d\mathbf{v}/dt$ is the particle acceleration and is given by

$$\mathbf{A} = D(\mathbf{u}_G - \mathbf{v}) - \frac{1}{\rho_s}\nabla_x p + \mathbf{g} - \frac{1}{\theta\rho_s}\nabla_x\tau, \qquad [5]$$

where D is a drag function, we use the expression of O'Rourke (1981):

$$D = C_d\frac{3}{8}\frac{\rho_G}{\rho_s}\frac{|\mathbf{u}_G - \mathbf{v}|}{r}, \qquad [6]$$

where

$$C_d = \frac{24}{\mathrm{Re}}\left(\epsilon^{-2.65} + \frac{\mathrm{Re}^{2/3}}{6}\epsilon^{-1.78}\right), \quad \mathrm{Re} = \frac{2\rho_G|\mathbf{u}_G - \mathbf{v}|r}{\mu_G}, \quad r = \left(\frac{m}{\frac{4}{3}\pi\rho_s}\right)^{1/3},$$

μ_G is the gas viscosity and ρ_s is the particle density. In the limit of $\epsilon = 1.0$, this drag formulation reduces to the Putnam (1961) correlation for solid spheres. The ϵ-dependence of C_d corresponds with that found in the experiments of Richardson & Zaki (1954). $\mathbf{g}$ is the gravitational acceleration.

In [5] τ is an isotropic solids stress for which we take the expression of Harris and Crighton (1994):

$$\tau = P_s\frac{\theta}{\theta_{cp} - \theta}, \qquad [7]$$

where P_s is a constant with units of pressure, θ is the particle-phase volume fraction, and θ_{cp} is the particle-phase volume fraction at close packing. As a first approximation, we assumed in [5] that the acceleration of an individual particle due to the solids stress is independent of size and velocity. When detailed theories have been developed that give the average collisional force on a particle as a function of size and velocity, this information can be incorporated into the MP-PIC formulation, providing a more detailed and fundamental approach to computing the solids stress.

The particle volume fraction θ is related to the distribution function f by

$$\theta = \int\int f \frac{m}{\rho_s} \, dm \, d\mathbf{v}. \qquad [8]$$

Then ϵ and θ are related by

$$\epsilon + \theta = 1.0. \qquad [9]$$

To complete the equations we need an expression for the interphase momentum transfer function $\mathbf{F}$:

$$\mathbf{F} = \int\int fm \left[D(\mathbf{u}_G - \mathbf{v}) - \frac{1}{\rho_s} \nabla \mathbf{p} \right] dm \, d\mathbf{v}. \qquad [10]$$

Note that when the second term in this integral is combined with the pressure gradient term in [2], and use is made of [8] and [9], a more familiar form of the gas momentum equation is obtained, in which ϵ multiplies the pressure gradient.

We now point out two ways in which the MP-PIC equations differ from usual multiphase flow formulations. First, the interphase momentum transfer function is more detailed than in continuum equation formulations. Typically, the latter take the momentum transfer rate to be proportional to the difference between the mass-averaged velocities of the phases (Risk 1993; Gidaspow 1986, 1994). Like particle/fluid models, the MP-PIC method solves for the distribution function f so we can compute the detailed $\mathbf{F}$ by summing contributions from particles of different velocities and sizes.

Second, the MP-PIC equations include the solids stress term in [5]. Many continuum phase formulations contain this term but particle/fluid models (Dukowicz 1980; O'Rourke 1981) ignore it because of limitations of the numerical methodology. Particle/fluid models do not include solids stress terms because they would have to implicitly couple the calculation of $\tau(\theta)$ on a grid with the motion of each individual particle, which would be very time-consuming computationally. The MP-PIC method overcomes this difficulty by solving continuum particle mass and momentum equations on the grid. Solution of these grid equations closely approximates what the solution would be if the individual particle equations of motion were implicitly coupled.

The mass and momentum equations for the particle phase that are implicitly solved by the MP-PIC method can be obtained by taking moments of [4]. By multiplying this equation successively by m and $m\mathbf{v}$ and integrating over the mass and velocity coordinates (Travis *et al.* 1976), we obtain:

$$\frac{\partial(\theta\rho_s)}{\partial t} + \nabla_{\mathbf{x}} \cdot (\theta\rho_s \mathbf{u}_s) = 0 \qquad [11]$$

and

$$\frac{\partial(\theta\rho_s \mathbf{u}_s)}{\partial t} + \nabla_{\mathbf{x}} \cdot (\theta\rho_s \mathbf{u}_s \mathbf{u}_s) + \nabla_{\mathbf{x}} \tau + \theta \nabla_{\mathbf{x}} p$$

$$= \theta\rho_s \mathbf{g} + \int\int fmD(\mathbf{u}_G - \mathbf{v}) \, dm \, d\mathbf{v} - \nabla_{\mathbf{x}} \cdot \left[\int\int fm(\mathbf{v} - \mathbf{u}_s)(\mathbf{v} - \mathbf{u}_s) \, dm \, d\mathbf{v} \right], \qquad [12]$$

where the mean particle velocity $\mathbf{u}_s$ is given by

$$\mathbf{u}_s = \frac{1}{\theta\rho_s} \int\int fm\mathbf{v} \, dm \, d\mathbf{v}, \qquad [13]$$

and we have used [5] and [8]. This derivation yields the form of the interphase momentum transfer rate and demonstrates that the solids stress term in the momentum equation is the same as that of Harris & Crighton (1994). It also shows that the MP-PIC equations account for the kinematic stress that arises from local particle velocity fluctuations about the mean velocity, the third term on the right of [12].

3. NUMERICAL SOLUTION OF THE MP-PIC EQUATIONS

We have written a computer program that solves the equations of the preceding section in one-dimensional Cartesian coordinates. In this section we give the finite difference approximations and numerical solution procedure used in this program. The gas-phase equations [1] and [2] are solved using an Eulerian grid finite difference scheme whose accuracy is first order in space and time. As in particle/fluid methods, the particle-phase equations are solved using computational parcels, each of which represents several physical particles of identical size, velocity and position. For clarity, we use the term "parcel" to refer to the computational entities to distinguish them from the physical particles. The computational parcels follow characteristic paths in the phase space whose coordinates are particle positions, velocities and sizes. As indicated above, we do not directly solve the particle- and gas-phase equations because this would involve a computationally costly, coupled and implicit solution for the motion of each particle. We instead interpolate the parcel properties onto the Eulerian grid and solve implicit approximations to particle-phase continuum equations that resemble [11] and [12] above. After the grid equations are solved, the local gas velocities, gas pressure gradients and solids stress gradients are interpolated back to the parcel positions and used in a final explicit update of parcel velocities. The MP-PIC method is a particle-in-cell method because it calculates particle interactions on a grid and achieves computational economy because there are fewer grid points than there are computational parcels. However, unlike most PIC methods, used for single-phase flows, the MP-PIC method parcels move with their own velocity rather than the mean particle velocity interpolated from the grid, so that multiphase interpenetration is allowed.

Finite difference approximations are defined using a grid of computational cells of uniform size Δx. We use a staggered mesh arrangement where gas thermodynamic variables are located at cell centers, with values at the center of cell "i" being denoted by subscript "i". The gas velocities and momentum densities are located at cell faces, with quantities at the right face of cell "i" being identified by subscript "$i+\frac{1}{2}$". A superscript "n" denotes the computed value of a variable at time $t = n\,\Delta t$, where Δt is the computational time step. The finite difference approximations to the gas continuity and momentum equations become

$$\frac{(\epsilon\rho_G)_i^{n+1} - (\epsilon\rho_G)_i^n}{\Delta t} + \frac{(\epsilon\rho_G u_G)_{i+1/2}^{n+1} - (\epsilon\rho_G u_G)_{i-1/2}^{n+1}}{\Delta x} = 0 \qquad [14]$$

and

$$\frac{(\epsilon\rho_G u_G)_{i+1/2}^{n+1} - (\epsilon\rho_G u_G)_{i+1/2}^n}{\Delta t} + \frac{(\epsilon\rho_G u_G^2)_{i+1}^n - (\epsilon\rho_G u_G^2)_i^n}{\Delta x} + \frac{\tilde{p}_{i+1} - \tilde{p}_i}{\Delta x} = -F_{i+1/2} - \frac{[(\epsilon\rho_G)_i^n + (\epsilon\rho_G)_{i+1}^n]g}{2}, \qquad [15]$$

where $\tilde{p}_i$ is a linearly implicit approximation to the advanced-time pressure p_i^{n+1} to be given later and $F_{i+1/2}$ is the approximation to the interphase momentum exchange term, also to be given later. An explicit, upwind approximation of the gas convective term keeps the system of equations linear:

$$(\epsilon\rho_G u_G^2)_i^n = \frac{m_{i-1/2} + m_{i+1/2}}{2} \cdot \begin{cases} (u_G)_{i-1/2}^n & \text{if} \quad m_{i-1/2} + m_{i+1/2} > 0 \\ (u_G)_{i+1/2}^n & \text{if} \quad m_{i-1/2} + m_{i+1/2} < 0 \end{cases} \qquad [16]$$

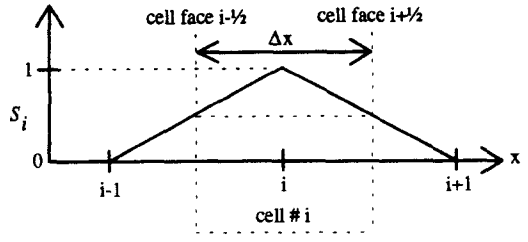

Figure 1. Linear interpolation function for domain cells.

where

$$m_{i+1/2} = (\epsilon\rho_G u_G)^n_{i+1/2} \text{ and } (u_G)^n_{i+1/2} = \frac{2(\epsilon\rho_G u_G)^n_{i+1/2}}{(\epsilon\rho_G)^n_i + (\epsilon\rho_G)^n_{i+1}}.$$

We use two types of functions to interpolate between the computational parcels and the Eulerian grid. For cell-centered variables we use the linear functions S_i in figure 1, which are equal to 1.0 at the centers of cells "i" and vary linearly to zero at the centers of the neighboring cells. For quantities located at cell faces, nearest-neighbor interpolation functions $T_{i+1/2}$ are used, where

$$T_{i+1/2} = \begin{cases} 1 & \text{if} \quad x_i \leqslant x < x_{i+1} \\ 0 & \text{if} \quad x < x_i \text{ or } x \geqslant x_{i+1} \end{cases} \qquad [17]$$

and x_i is the center of cell "i". It may readily be verified that

$$\frac{\partial S_i}{\partial x} = \frac{1}{\Delta x}(T_{i-1/2} - T_{i+1/2}), \qquad [18]$$

a fact used later when we derive the discretized particle continuum equations on the grid. The value of an interpolation function at a parcel's position can be thought of as the fraction of some parcel property that belongs to an Eulerian cell.

Each computational parcel represents a number N_p of real particles with identical mass m_p, velocity v_p and position x_p. The Liouville equation [4] is the mathematical expression of conservation of particle numbers in volumes moving along dynamic trajectories in particle phase space. Thus, the number of particles N_p associated with a parcel is constant in time. Because we assume no mass exchange between phases, the particle mass m_p is also constant. Parcel positions and velocities are updated using the following implicit approximations:

$$x_p^{n+1} = x_p^n + v_p^{n+1}\Delta t \qquad [19]$$

and

$$\frac{v_p^{n+1} - v_p^n}{\Delta t} = -g - \frac{1}{\rho_s}\left(\frac{\tilde{p}_{i+1} - \tilde{p}_i}{\Delta x}\right)_p - \frac{1}{\rho_s\theta_p}\left(\frac{\tilde{\tau}_{i+1} - \tilde{\tau}_i}{\Delta x}\right)_p + D_p(\tilde{u}_{G,p} - v_p^{n+1}). \qquad [20]$$

Implicit approximations are used to overcome time step stability restrictions that would cause computational inefficiency. Equation [20] introduced various new notations and we now give detailed definitions.

The pressure $\tilde{p}_i$ is the same linearity implicit approximation to the advanced-time gas pressure used in the gas-phase momentum equation [15]. This pressure is given by

$$\tilde{p}_i = p_i^n\left\{1 + \gamma\left[\frac{(\epsilon\rho_G)_i^{n+1} - (\epsilon\rho_G)_i^n}{(\epsilon\rho_G)_i^n} + \frac{\tilde{\theta} - \theta_i^n}{1 - \theta_i^n}\right]\right\}, \qquad [21]$$

where the time-n pressure is

$$p_i^n = p_{\text{ref}}\left[\frac{(\epsilon\rho_G)_i^n}{(1-\theta_i^n)\rho_{G,\text{ref}}}\right]^\gamma. \tag{22}$$

p_{ref} and $\rho_{G,\text{ref}}$ are values of the gas pressure and density at some reference state. The time-n particle volume fraction is

$$\theta_i^n = \frac{1}{\Delta x}\sum_{\text{p}} S_i(x_p^n)\frac{m_{\text{p}}}{\rho_{\text{s}}}N_{\text{p}}, \tag{23}$$

and $\tilde{\theta}_i$ is an approximation to the advanced-time particle volume fraction given later. Equation [21] is derived by noting that the pressure is a function of our dependent variables $\epsilon\rho_G$ and θ and linearizing about the time-n values of these variables.

In [20] the subscript p denotes that a quantity is evaluated at a provisional parcel position given by

$$\tilde{x}_{\text{p}} = x_{\text{p}}^n + v_{\text{p}}^n\,\Delta t \tag{24}$$

and evaluated using the cell-face interpolation functions $T_{i+1/2}$. For example,

$$\left(\frac{\tilde{p}_{i+1}-\tilde{p}_i}{\Delta x}\right)_{\text{p}} = \sum_i T_{i+1/2}(\tilde{x}_{\text{p}})\frac{\tilde{p}_{i+1}-\tilde{p}_i}{\Delta x}. \tag{25}$$

Analogously, in [20] $\tilde{\tau}_i$ is a linearly implicit approximation to the advanced-time solids stress defined by

$$\tilde{\tau}_i = P_{\text{s}}\frac{\theta_{\text{cp}}}{(\theta_{\text{cp}}-\theta_i^n)^2}(\tilde{\theta}_i-\theta_i^n)+\tau_i^n. \tag{26}$$

The volume fraction θ_{p} in [20] is based on the provisional parcel positions:

$$\theta_{\text{p}} = \sum_i T_{i+1/2}(\tilde{x}_{\text{p}})\theta_{i+1/2}, \tag{27a}$$

where

$$\theta_{i+1/2} = \frac{1}{\Delta x}\sum_{\text{p}} T_{i+1/2}(\tilde{x}_{\text{p}})N_{\text{p}}\frac{m_{\text{p}}}{\rho_{\text{s}}}. \tag{27b}$$

We now verify that our differencing of the solids stress term in [20] conserves total particle momentum. Multiplying [20] by $N_{\text{p}}m_{\text{p}}$ and summing over all parcels results in

$$\sum_{\text{p}} N_{\text{p}}m_{\text{p}}\frac{v_{\text{p}}^{n+1}-v_{\text{p}}^n}{\Delta t} = \cdots - \sum_{\text{p}}\frac{N_{\text{p}}m_{\text{p}}}{\rho_{\text{s}}\theta_{\text{p}}}\left(\frac{\tilde{\tau}_{i+1}-\tilde{\tau}_i}{\Delta x}\right)_{\text{p}}, \tag{28}$$

where we omitted all terms on the right-hand side of the resulting equation except the last. By using the definition of $[(\tilde{\tau}_{i+1}-\tilde{\tau}_i)/\Delta x]_{\text{p}}$, interchanging the order of summations over parcels and cells, and noting that $\theta_{\text{p}} = \theta_{i+1/2}$ if and only if $T_{i+1/2}(\tilde{x}_{\text{p}}) = 1$ (see [27a]), we obtain

$$\sum_{\text{p}} N_{\text{p}}m_{\text{p}}\frac{v_{\text{p}}^{n+1}-v_{\text{p}}^n}{\Delta t} = \cdots - \sum_i\left[\sum_{\text{p}}\frac{N_{\text{p}}m_{\text{p}}}{\rho_{\text{s}}}T_{i+1/2}(\tilde{x}_{\text{p}})\right]\frac{\tilde{\tau}_{i+1}-\tilde{\tau}_i}{\theta_{i+1/2}\,\Delta x}. \tag{29}$$

Using the definition of $\theta_{i+1/2}$ in [27b], we see the sum in [29] is zero, except for possible boundary sources and thus proving conservation.

The last term in [20] is the drag term based on a linearly implicit approximation to the advanced-time gas velocity u_G:

$$\tilde{u}_{G,\text{p}} = \sum_i T_{i+1/2}(\tilde{x}_{\text{p}})\frac{2(\epsilon\rho_G u_G)_{i+1/2}^{n+1}}{(\epsilon\rho_G)_i^n + (\epsilon\rho_G)_{i+1}^n}. \tag{30}$$

The approximation to the particle drag function, [6], uses the time-n value of the parcel velocity and the following approximations to ρ_G, u_G and ϵ at the parcel position:

$$\rho_{G,\mathrm{p}} = \sum_i S_i(\tilde{x}_\mathrm{p}) \frac{(\epsilon\rho_G)_i^n}{1-\theta_i^n} \tag{31}$$

$$u_{G,\mathrm{p}} = \sum_i T_{i+1/2}(\tilde{x}_\mathrm{p}) \frac{2(\epsilon\rho_G u_G)_{i+1/2}^n}{(\epsilon\rho_G)_i^n + (\epsilon\rho_G)_{i+1}^n} \tag{32}$$

and

$$\epsilon_\mathrm{p} = \begin{cases} \sum_i T_{i+1/2}(\tilde{x}_\mathrm{p})(1-\theta_{i+1}^n) & \text{if} \quad v_\mathrm{p}^n > 0 \\ \sum_i T_{i+1/2}(\tilde{x}_\mathrm{p})(1-\theta_i^n) & \text{if} \quad v_\mathrm{p}^n \leqslant 0. \end{cases} \tag{33}$$

Having introduced approximations to the particle acceleration equation, we now give the difference approximation to the momentum exchange term:

$$F_{i+1/2} = \left\{ \sum_\mathrm{p} T_{i+1/2}(\tilde{x}_\mathrm{p}) \left[D_\mathrm{p}(\tilde{u}_{G,\mathrm{p}} - v_\mathrm{p}^{n+1}) - \frac{1}{\rho_\mathrm{s}} \left(\frac{\tilde{p}_{i+1} - \tilde{p}_i}{\Delta x} \right)_\mathrm{p} \right] N_\mathrm{p} m_\mathrm{p} \right\} \Big/ \Delta x. \tag{34}$$

By multiplying [20] by $N_\mathrm{p} m_\mathrm{p}$, summing the resulting equation over all pacels, and using [34], it is easily verified that momentum is conserved in the calculation of momentum exchange between the phases.

The heart of the MP-PIC method is in the use of the as yet undefined particle volume fraction $\tilde{\theta}_i$ in [21] and [26] to approximate advanced-time pressures and solids stresses. If in place of $\tilde{\theta}_i$ we had used θ_i^{n+1}, which depends on all the advanced-time parcel positions, we would have had a closed system of equations coupling the motion of all the parcels with that of the gas. However, this system would be extremely time-consuming to solve because of the large number of unknowns that are implicitly coupled. We reduce the number of unknowns by solving for a $\tilde{\theta}_i$ that closely approximates θ_i^{n+1}. The MP-PIC formulation has continuity and momentum equations for each phase, discretized on the grid, which eliminates the unknown parcel velocities v_p^{n+1} from these equations. Once the grid quantities are solved, the parcel velocities and positions are updated explicitly. We now derive the MP-PIC grid equations.

The derivation has three steps. First, the advanced-time parcel velocities are eliminated from the gas momentum equation. The following equation for v_p^{n+1} results from a simple rearrangement of [20]:

$$v_\mathrm{p}^{n+1} = \frac{v_\mathrm{p}^n + \Delta t \left[D_\mathrm{p}\tilde{u}_{G,\mathrm{p}} - g - \frac{1}{\rho_\mathrm{s}} \left(\frac{\tilde{p}_{i+1} - \tilde{p}_i}{\Delta x} \right)_\mathrm{p} - \frac{1}{\rho_\mathrm{s}\theta_\mathrm{p}} \left(\frac{\tilde{\tau}_{i+1} - \tilde{\tau}_i}{\Delta x} \right)_\mathrm{p} \right]}{1 + \Delta t D_\mathrm{p}}. \tag{35}$$

By using [35] to eliminate v_p^{n+1} from [34], substituting from the resulting equation to eliminate $F_{i+1/2}$ in [15], and doing some algebraic manipulation, we obtain the following gas-phase momentum equation:

$$\frac{(\epsilon\rho_G u_G)_{i+1/2}^{n+1} - (\epsilon\rho_G u_G)_{i+1/2}^n}{\Delta t} + \frac{(\epsilon\rho_G u_G^2)_{i+1}^n - (\epsilon\rho_G u_G^2)_i^n}{\Delta x} + (1 - C_{i+1/2}) \frac{\tilde{p}_{i+1} - \tilde{p}_i}{\Delta x}$$

$$= -A_{i+1/2}(\epsilon\rho_G u_G)_{i+1/2}^{n+1} + B_{i+1/2} - D_{i+1/2} \frac{\tilde{\tau}_{i+1} - \tilde{\tau}_i}{\Delta x} - \frac{(\epsilon\rho_G)_i^n + (\epsilon\rho_G)_{i+1}^n}{2} g. \tag{36}$$

The coefficients $A_{i+1/2}$, $B_{i+1/2}$, $C_{i+1/2}$ and $D_{i+1/2}$ are given in appendix A and depend only on explicitly known information. It is worth noting that the C coefficient is an approximation to θ and so the coefficient of the pressure gradient in [36] is an approximation to the gas volume fraction ϵ.

The second step in the derivation is to obtain the particle-phase continuity equation. By taking the difference between [23] evaluated at time levels $n+1$ and n we obtain

$$\theta_i^{n+1} - \theta_i^n = \frac{1}{\Delta x} \sum_{\mathrm{p}} [S_i(x_{\mathrm{p}}^{n+1}) - S_i(x_{\mathrm{p}}^n)] \frac{m_{\mathrm{p}} N_{\mathrm{p}}}{\rho_{\mathrm{s}}}. \qquad [37]$$

The value of the interpolation function at x_{p}^{n+1} is given approximately by

$$S_i(x_{\mathrm{p}}^{n+1}) \approx S_i(\tilde{x}_p) + (x_{\mathrm{p}}^{n+1} - \tilde{x}_{\mathrm{p}}) \frac{\partial S_i}{\partial x}(\tilde{x}_{\mathrm{p}}), \qquad [38]$$

where $\tilde{x}_{\mathrm{p}}$ is defined in [24]. The equation for the approximate volume fraction $\tilde{\theta}_i$ is obtained by substituting the right-hand side of [38] for $S_i(x_{\mathrm{p}}^{n+1})$ in [37] and using [18]:

$$\frac{\tilde{\theta}_i - \theta_i^n}{\Delta t} + \left.\frac{\partial(\theta u_{\mathrm{s}})}{\partial x}\right|_{\text{explicit}} + \frac{(\theta\, \delta u_{\mathrm{s}})_{i+1/2} - (\theta\, \delta u_{\mathrm{s}})_{i-1/2}}{\Delta x} = 0, \qquad [39]$$

where

$$\left.\frac{\partial(\theta u_{\mathrm{s}})}{\partial x}\right|_{\text{explicit}} = \frac{1}{\Delta x} \sum_{\mathrm{p}} \left[\frac{S_i(x_{\mathrm{p}}^n) - S_i(\tilde{x}_{\mathrm{p}})}{\Delta t}\right] \frac{m_{\mathrm{p}} N_{\mathrm{p}}}{\rho_{\mathrm{s}}} \qquad [40]$$

and

$$(\theta\, \delta u_{\mathrm{s}})_{i+1/2} = \frac{1}{\Delta x} \sum_{\mathrm{p}} \frac{m_{\mathrm{p}} N_{\mathrm{p}}}{\rho_{\mathrm{s}}} T_{i+1/2}(\tilde{x}_{\mathrm{p}})(v_{\mathrm{p}}^{n+1} - v_{\mathrm{p}}^n). \qquad [41]$$

Equation [39] for the particle phase volume fraction has one term that depends on the advanced-time particle velocities. Step three of the derivation consists of using [35] to eliminate v_{p}^{n+1} from [41] to obtain an equation for $(\theta\, \delta u_{\mathrm{s}})_{i+1/2}$ that depends only on grid quantities:

$$\rho_{\mathrm{s}} \frac{(\theta\, \delta u_{\mathrm{s}})_{i+1/2}}{\Delta t} = A_{i+1/2}(\epsilon \rho_G u_G)_{i+1/2}^{n+1} - C_{i+1/2} \frac{\tilde{p}_{i+1} - \tilde{p}_i}{\Delta x} - E_{i+1/2} \frac{\tilde{\tau}_{i+1} - \tilde{\tau}_i}{\Delta x} - F_{i+1/2}, \qquad [42]$$

where the coefficients $E_{i+1/2}$ and $F_{i+1/2}$ are given in appendix A and depend only on explicitly known information.

Equations [14], [36], [39] and [42] are the MP-PIC continuity and momentum equations for the gas- and particle-phases. These comprise a system of four linear equations for the unknowns θ, $\theta\, \delta u_{\mathrm{s}}$, $\epsilon \rho_G$ and $\epsilon \rho_G u_G$. Coefficients A, B, C, D, E and F are explicitly calculated. When [36] and [42] are used to eliminate $\theta\, \delta u_{\mathrm{s}}$ and $\epsilon \rho_G u_G$ from [14] and [39], two equations are obtained per cell relating the unknown θ and $\epsilon \rho_G$ to their neighbors and themselves. These two coupled equations are solved by holding the current approximation for each variable fixed and solving the equation for the other variable by a tridiagonal matrix solver, and repeating this procedure while alternating the fixed and solution variables until convergence is obtained. After convergence, $\theta\, \delta u_{\mathrm{s}}$ and $\epsilon \rho_G u_G$ are calculated from [36] and [42]. Finally, [19] and [20] are used to calculate the final particle velocities and positions.

Note that the only approximation used in obtaining the particle-phase grid equations from the particle equations is the use of [38]. The difference between the left- and right-hand sides of [38] is of order Δt^4, and thus $\tilde{\theta}_i$ is expected to be a very good approximation to θ_i^{n+1}. Significant differences between these two quantities might be expected to introduce numerically-generated wave motions or convergence difficulties, but we experienced no such difficulties obtaining the example solutions in the next section.

4. TEST PROBLEMS

Six test problems for the MP-PIC method are described and solved. These test problems have been chosen either because they demonstrate the accuracy of the method or because they have analytical solutions for comparison purposes. The first test problem computes the speed of a sound wave in a multiphase mixture. The second computes the speed of a stress wave driven by the solids stress term. The third problem computes the sedimentation of a dispersed (low volume fraction)

Table 1. Physical parameters for all test problems

Gas density (kg/m^3)	1.0
Gas viscosity (kg/ms)	2.0×10^{-2}
Solid density (kg/m^3)	10^3
Gravity (g) (m/s^2)	9
Particle mass (kg)	$4{\cdot}188 \times 10^{-6}$
Particle radius (m)	10^{-3}
γ	1·4

slug of particles. The dispersed slug shows some interesting accuracy results about the MP-PIC method and serves to introduce more general analytical solutions for sedimentation problems. The fourth, fifth and sixth problems simulate sedimentation of dense particulate slugs having one, two and three particle sizes, respectively.

The first five test problems use the same gas properties and particle size given in table 1, chosen for convenient non-dimensionalization and a low particle Reynolds number of 10^{-2}. This low Re is not an inherent limitation of the method but simplifies the drag coefficient because the $Re^{2/3}$ terms may be neglected. The last test problem compares with experiments measuring sedimentation of mixtures of three particle sizes. In this problem it is important to retain the $Re^{2/3}$ term in the drag coefficient.

5. SPEED OF SOUND

The speed of sound in a multiphase mixture with velocity equilibrium between phases is given by the following (Wallis 1969; Gidaspow 1986):

$$\frac{1}{c_m^2} = \rho_m\left(\frac{\epsilon}{\rho_G c_G^2} + \frac{\theta}{\rho_s c_s^2}\right), \quad \text{with } \rho_m = \epsilon\rho_G + \theta\rho_s.$$

We have $c_s^2\rho_s \gg c_G^2\rho_G$ and $\epsilon\rho_m \simeq \epsilon\theta\rho_s$, giving:

$$c_m = c_G\sqrt{\frac{\rho_G}{\epsilon\theta\rho_s}} \text{ with } c_G^2 = \frac{\gamma p}{\rho_G}. \qquad [43]$$

To compute c_m we impose a sinusoidal half-wavelength gas and particle velocity perturbation as shown in figure 2.

The solids volume fraction is set at 0.2 and to ensure the particles follow the gas velocity the drag coefficient is set to a large value of 10^{20}. The solids stress term is neglected by setting $P_s = 0$. Table 2 gives additional computational details.

From the problem specifications the gas sound speed is $c_G = 374.2$ (m/s) and the mixture speed is $c_m = 29.56$ (m/s).

The mixture speed corresponds to a pressure wave oscillation time $\tau = \lambda/c_m = 6.766 \times 10^{-2}$ (s), and with a time step of 3×10^{-3} (s) and cell size of 1/40 (m), the corresponding numerical Courant number is 3.55. To observe the pressure oscillation that accompanies the speed of sound, we plot

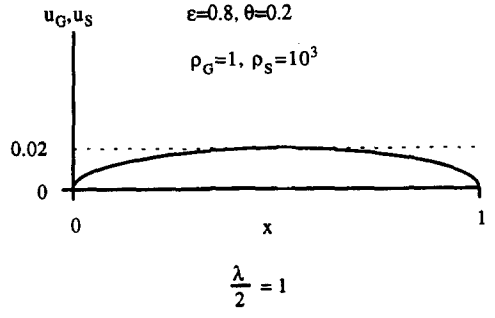

Figure 2. Initial conditions for the speed of sound in a mixture.

Table 2. Computational details for the sound wave test problem

Length of domain (m)	1
Gas perturbation velocity (m/s)	0.02
Number of particles per parcel	95,500
Number of computational cells	40 or 80
Time step (s)	1.5×10^{-3} or 3×10^{-3}
Number of parcels	500
Reference pressure p_{ref} (N/m^2)	10^5

the pressure at the center cell $x = \lambda/4$ in figure 3. Inspection of the figure reveals a computed oscillation period of 6.77×10^{-2} (s), which is in excellent agreement with the analytical result. The pressure wave in figure 3 is numerically damped due to the implicit nature of our numerical method and the large Courant numbers used in this calculation. A numerical stability analysis by O'Rourke (1985) yielded the following amplification reduction factor, A, per time step of

$$A = \frac{1}{\sqrt{1 + 4c^2 \sin^2\left(\frac{\psi}{2}\right)}}, \quad \text{with } \psi = \frac{2\pi}{\lambda} \cdot \Delta x$$
$$\text{and } c = \frac{c_m \Delta t}{\Delta x}. \qquad [44]$$

Inserting values for the case with $NX = 40$ ($\Delta x = 1/NX$) and $\Delta t = 3 \times 10^{-3}$ (s), gives a reduction of 0.9633 per time step. Since one pressure oscillation corresponds to approximately 22.5 time steps, the expected amplitude reduced between oscillations is $(0.9633)^{22.5}$, a factor of 0.4314. Measuring the reduction from figure 3 gives a value of 0.4135, which is in excellent agreement with the numerical stability result.

6. SPEED OF A STRESS WAVE

Gidaspow (1986) gave an analytical solution for the propagation speed of a small density fluctuation for a dense particulate flow in a vacuum. The wave is propagated by the particle stress term that may be written as

$$\frac{\partial \tau_s}{\partial x} = G(\theta_0) \frac{\partial \theta}{\partial x}, \quad G(\theta_0) = \frac{P_s \theta_{cp}}{(\theta_{cp} - \theta_0)^2} \qquad [45]$$

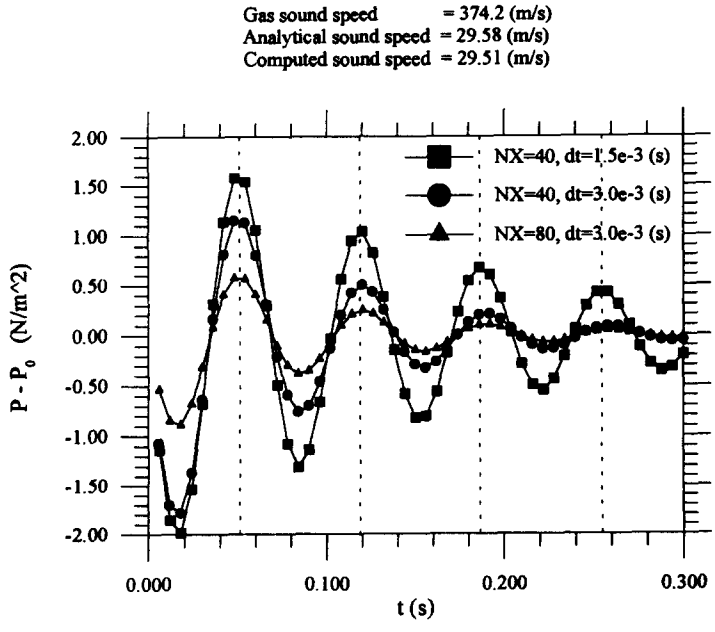

Figure 3. Pressure at the center point for the speed of sound test problem.

Table 3. Stress wave test problem

Initially	$u_G = u_p = 0$, $\theta_0 = 0.2$
Reference pressure (p_{ref})	10^6
$C_d = 0$, $P_s = 5.0$	
Time step (s)	2×10^{-3}, 10^{-2}, 2×10^{-2}
Number of parcels	200
Particles/parcel	238,750 and 243,525
Number of computational cells	40 and 80
Length of domain (m)	1

where θ_0 is the reference solid volume fraction. We reproduced the necessary conditions to propagate such a stress wave by setting the drag coefficient to zero and, thus, decoupling the particles from the gas. Gas velocities are small and so the pressure gradient is negligible. The particle phase equations may be readily reduced to the form (Gidaspow 1986):

$$\frac{\partial^2\theta}{\partial t^2} = \frac{G(\theta_0)}{\rho_s}\frac{\partial^2\theta}{\partial x^2}, \quad c_c = \sqrt{\frac{G(\theta_0)}{\rho_s}} \qquad [46]$$

with the stress wave speed c_c. Table 3 gives the test problem specification. Figure 4 shows that a reference solids volume fraction of 0.2 is used and a small volume fraction step of 2% of θ_0 is specified at the center of the domain.

Inserting the problem specification values in [46] gives a stress wave speed $c_c = 0.1183$ (m/s). Figure 5 shows the results from the calculation with the continuity differential $\theta - \theta_0$ plotted against x. As might be expected, the figure shows two oppositely moving waves with a region of high wave number harmonics between. The envelope described by the expanding waves grows linearly with time. Figure 6 plots the separation distance measured from $-\theta'/4$ to $\theta'/4$ against time and the analytical solution. The rate of increase in separation gives the computed wave speed as 0.1176 (m/s), which is in excellent agreement with the analytical result of 0.1183 (m/s).

7. FALL OF A DISPERSED SLUG OF PARTICLES

This test problem considers the fall of a particle slug where the particles are dispersed to give a low solids volume fraction ($\theta_0 = 5.22 \times 10^{-4}$). Table 4 gives details of the initial conditions and computational parameters.

It is convenient at this point to introduce some analytical results. The low solids volume fraction means that the gas volume fraction ϵ is close to 1, and so the solid stresses and the volume fraction dependence of the drag coefficient can be neglected. We first seek a solution where there are no spatial gradients, other than pressure gradients developed in the slug and, consequently, where all particles fall with a velocity u_s that depends on time alone. With these assumptions the gas and particle momentum equations can be written:

$$\epsilon\frac{\partial u_G}{\partial t} + \frac{\epsilon}{\rho_G}\frac{\partial p}{\partial x} = -\epsilon g - D_s\theta\frac{\rho_s}{\rho_G}(u_G - u_s)$$

$$\theta\frac{\partial u_s}{\partial t} + \frac{\theta}{\rho_s}\frac{\partial p}{\partial x} = -\theta g + D_s\theta(u_G - u_s) \qquad [47]$$

with a Stokes time scale $1/D_s = 2\rho_s r^2/9\mu_G$.

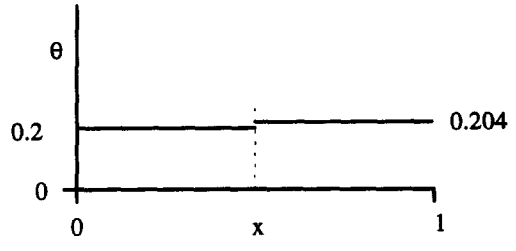

Figure 4. Initial conditions for the speed of a stress wave.

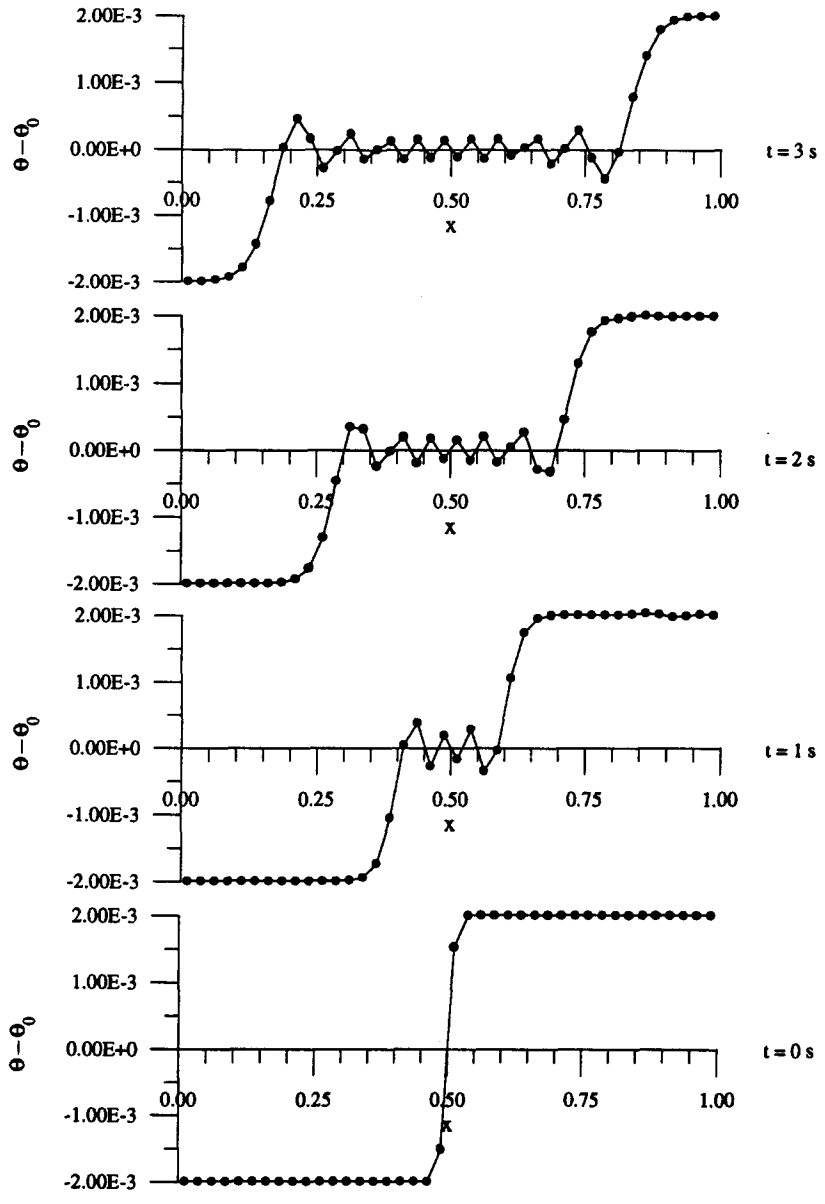

Figure 5. Computed solid volume fraction profiles for a stress wave.

Since the flow is incompressible, ρ_G is a constant. Adding the gas and solids continuity equations [1] and [11], and using the boundary conditions that velocities are zero at the top and bottom walls gives:

$$\theta u_s + \epsilon u_G = 0. \qquad [48]$$

Using [48] and eliminating the pressure gradient between the equations in [47] gives the following formulas for particle and gas velocities starting from initially stationary positions:

$$u_s = \frac{\epsilon^2 g}{D_s}\left(\frac{\rho_G - \rho_s}{\rho_s}\right)\left[1 - \exp\left(-\frac{D_s \rho_s}{\epsilon(\theta\rho_G + \epsilon\rho_s)}t\right)\right], \text{ and } u_G = -\frac{\theta v_p}{\epsilon}. \qquad [49]$$

This expression reduces to a single particle result for $\epsilon = 1$ and $\theta = 0$. For the present problem, the Stokes time scale $1/D_s$ is 1/90 (s) and the particle has a free fall velocity of $v_\infty = -0.1$ (m/s).

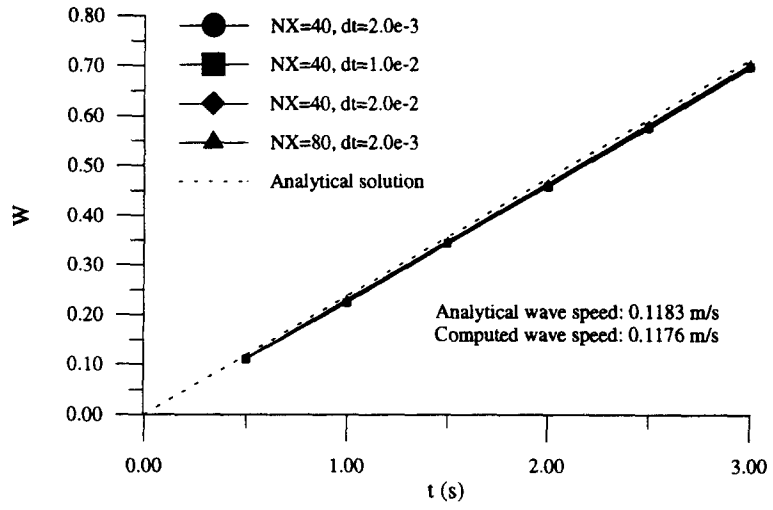

Figure 6. The computed spread of a stress wave.

Thus, the separation velocity of the slug and gas rapidly reaches a constant value and the slug fall obeys a drift flux model so that:

$$\Delta u = u_G - u_s = \text{constant} > 0. \qquad [50]$$

More generally, we now show the sedimenting slug can develop spatial inhomogeneities. The drift flux approximation [50] is still good since relaxation times to the constant separation velocity are small compared with sedimentation times. Using [48] and [50] we find $u_G = \theta\, \Delta u$ and $u_s = -\epsilon\, \Delta u$, and the solids continuity equation may be written as:

$$\frac{\partial \theta}{\partial t} + \Delta u(2\theta - 1)\frac{\partial \theta}{\partial x} = 0. \qquad [51]$$

This may be solved by the method of characteristics to give the results in figure 7:

$$\theta = \frac{1}{2}\left(1 + \frac{x}{\Delta u t}\right) \quad \text{for } \Delta u(2\theta_{-\infty} - 1)t \leqslant x \leqslant \Delta u(2\theta_{+\infty} - 1)t$$

$$= \theta_{-\infty} \qquad \text{for } x \leqslant \Delta u(2\theta_{-\infty} - 1)t$$

$$= \theta_{+\infty} \qquad \text{for } x \geqslant \Delta u(2\theta_{+\infty} - 1)t. \qquad [52]$$

In the present dispersed slug problem $\theta_{-\infty} = 0$ and $\theta_{+\infty} = \theta_0 = 5.22 \times 10^{-4}$ so from [52] the initial step gradient on the lower side of the slug remains steep throughout the calculation.

The step function profile of the upper part of the slug remains unchanged. This is because the characteristic velocity $\Delta u(2\theta - 1)$ of [51] is an increasing function of θ. Thus, characteristics emanating from the low θ region above the slug cross characteristics emanating from within the slug and form a kinematic "shock" moving with velocity $\Delta u = v_\infty$. Kynch (1952) previously obtained this result. Physically what happens is that if a particle falls behind the slug it finds itself in a region of lower θ, where the gas velocity is smaller, and the particle catches up with the slug.

Table 4. Computational details for the fall of a dispersed slug of particles

Initially	$u_G = u_p = 0$, $\theta_0 = 5.22 \times 10^{-4}$
Time step (s)	10^{-3}
Number of parcels	250
Number of computational cells	25
Length of domain (m)	1
Number of particles per parcel	100
Initial position of parcels	Uniform spacing between 0.6 and 0.8 m (cells 16–20)

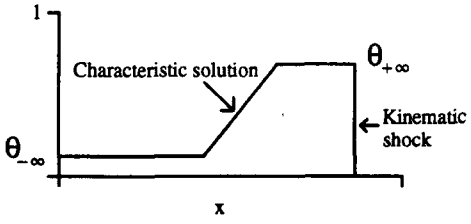

Figure 7. Analytical solution for sedimentation.

The above analysis revealed that we expect the dispersed slug to fall at the terminal velocity v_∞ and preserve its initial step shape throughout the motion. Such a problem is a useful test of numerical diffusion. Furthermore, our analysis also revealed that with a drift flux approximation a linear mixing region should form below the slug that penetrates the gas with the terminal velocity v_∞ and with a dense slug velocity of $v_{\text{slug}} = -\epsilon\,\Delta u$. This characteristics analysis provides an analytical solids volume fraction profile [52], for low solid volume fraction.

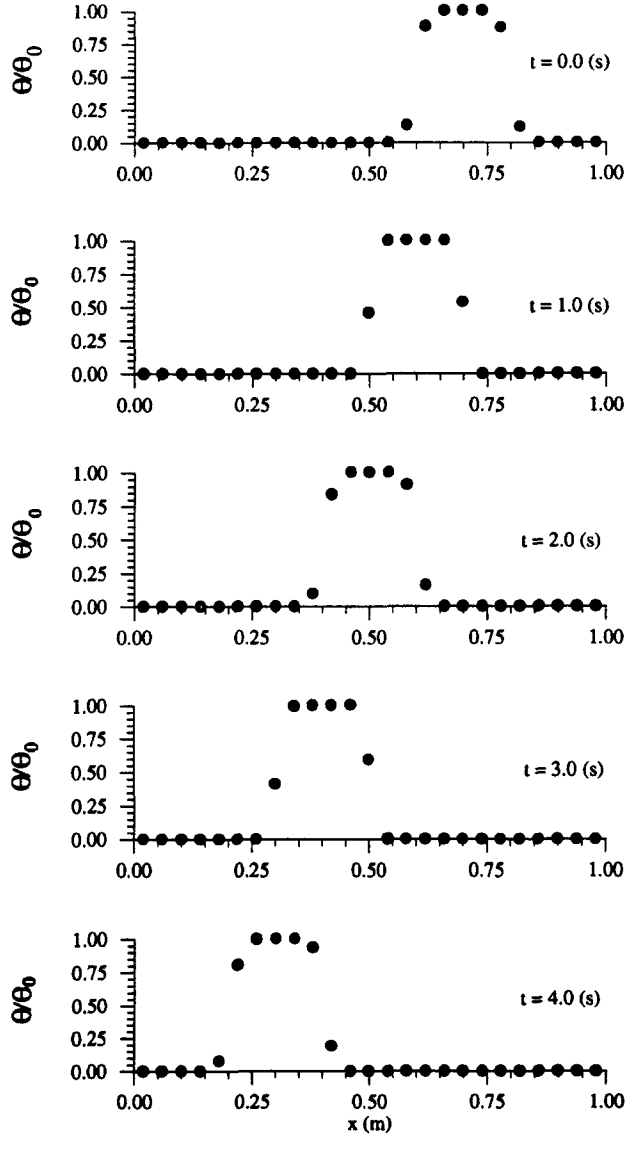

Figure 8. Computed solid volume fraction of a falling disperse slug of particles.

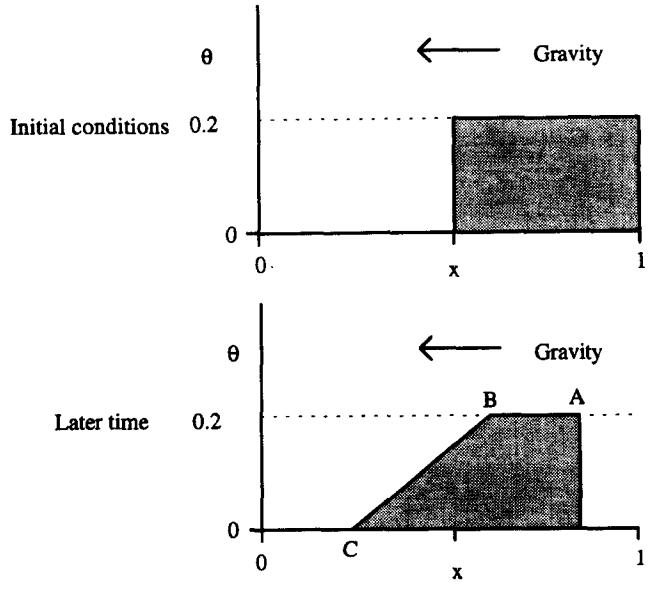

Figure 9. Solids volume fraction for the sedimentation of a granular mixture.

Figure 8 shows the computed time development of the dispersed slug problem with the solids volume fraction normalized by θ_0. The figure shows that the edges of the volume fraction are rounded because of the linear interpolation S function, shown in figure 1. The slug falls at a computed constant velocity of 0.0991 (m/s), which is in excellent agreement with the expected value of 0.1 (m/s).

Since the computational cell size is 0.04 (m) and the slug velocity is close to 0.1 (m/s), the slug traverses five computational cells in a time of 2 (s). Therefore, the solids volume fraction plots in figure 8 should be the same at 0, 2 and 4 (s), and at 1 and 3 (s). Inspection of the figure reveals that the slug profile at 2 and 4 (s) and 1 and 3 (s) are practically identical. A small difference can be seen between 0 and 2 (s). This may be attributed to the finite rise time of the slug velocity to its free-fall value. This accurate retention of the solids volume fraction profile as it moves across the grid shows that the MP-PIC calculation has low numerical diffusion because of its particle nature.

8. SEDIMENTATION OF A GRANULAR MIXTURE

This test problem considers the sedimentation of a densely packed granular mixture comprised of particles of a single size. Figure 9 shows that the initial solids volume fraction distribution fills the top half of the computational domain with a solids volume fraction of 0.2. Table 5 gives other details of the problem. Since the particle and gas properties are the same as the previous problem, the maximum velocity of a particle is the free-fall value of -0.1 (m/s). This test problem offers significant difficulties because of the volume fraction dependence in the drag function. Using the drift flux approximation, we obtain the following expression for the mixture separation velocity, Δu_m, when pressure is eliminated from the momentum equations:

$$\Delta u_m = \epsilon^n \Delta u = \epsilon^n g/D_s, \text{ with } n = 3.65 \text{ and } \rho_s \gg \rho_G. \quad [53]$$

Table 5. Computational details for the sedimentation of a granular mixture

Number of particles per parcel	119,370
Number of parcels	200
Number of computational cells	40
Time step (s)	2×10^{-3}
Length of computational domain (m)	1
Initial position of parcels	Uniform spacing between 0.5 and 1 m

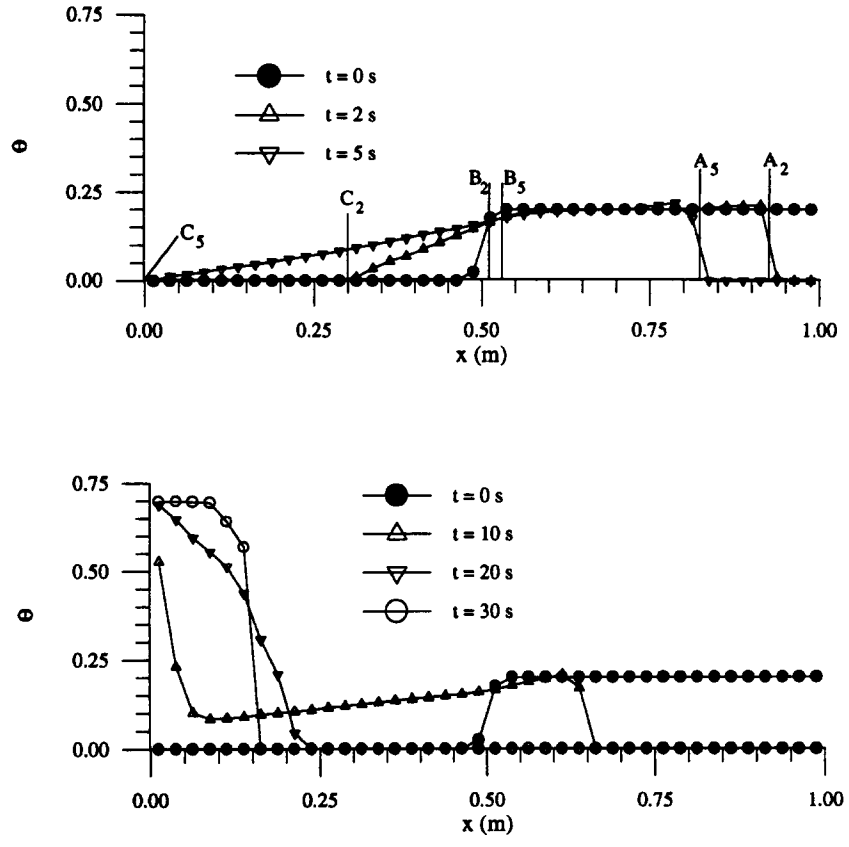

Figure 10. Computed solids volume fraction at early and late times for granular sedimentation.

The solids stress has been neglected as part of the drift flux approximation. In the limit of a single particle, $\epsilon \simeq 1$ and $\Delta u_m \simeq \Delta u = 0.1$ (m/s). However, for the present problem, the ϵ dependence gives $\Delta u_m = 0.0443$ (m/s).

The solids volume fraction equation is now modified to:

$$\frac{\partial \theta}{\partial t} + \Delta u_m((2+n)\theta - 1)\frac{\partial \theta}{\partial x} = 0. \qquad [54]$$

The solution to [54] at the low end of the slug is

$$\theta = \begin{cases} v^{-1}\left(\dfrac{x}{t}\right) & v(\theta_{-\infty})t \leqslant x \leqslant v(\theta_{+\infty})t \\ \theta_{-\infty} & x \leqslant v(\theta_{-\infty})t \\ \theta_{+\infty} & x \geqslant v(\theta_{+\infty})t, \end{cases}$$

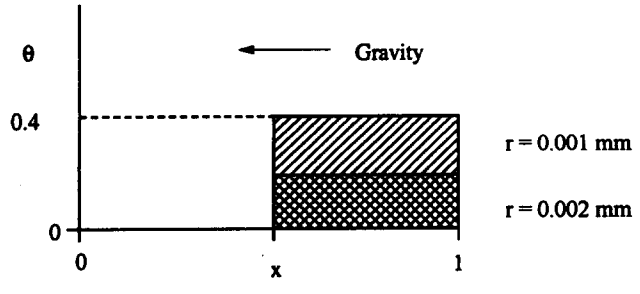

Figure 11. Initial conditions for the binary separation test problem.

Table 6. Computational details for the separation of a binary mixture

Small particle radius (mm)	1
Number of small particles per parcel	47,760
Number of parcels with small particles	250
Large particle radius (mm)	2
Number of small particles per parcel	5970
Number of parcels with large particles	250
Number of computational cells	50
Time step (s)	5×10^{-4}
Length of computational domain (m)	1
Initial position of parcels	Uniform spacing between 0.5 and 1 m

where $v(\theta)$ is the characteristics velocity $\Delta u_m[(2+n)\theta - 1]$ and v^{-1} is the inverse function (i.e. $v^{-1}(v(\theta)) = \theta$). The upper part of the slug will again remain a step function because of the crossing of characteristics.

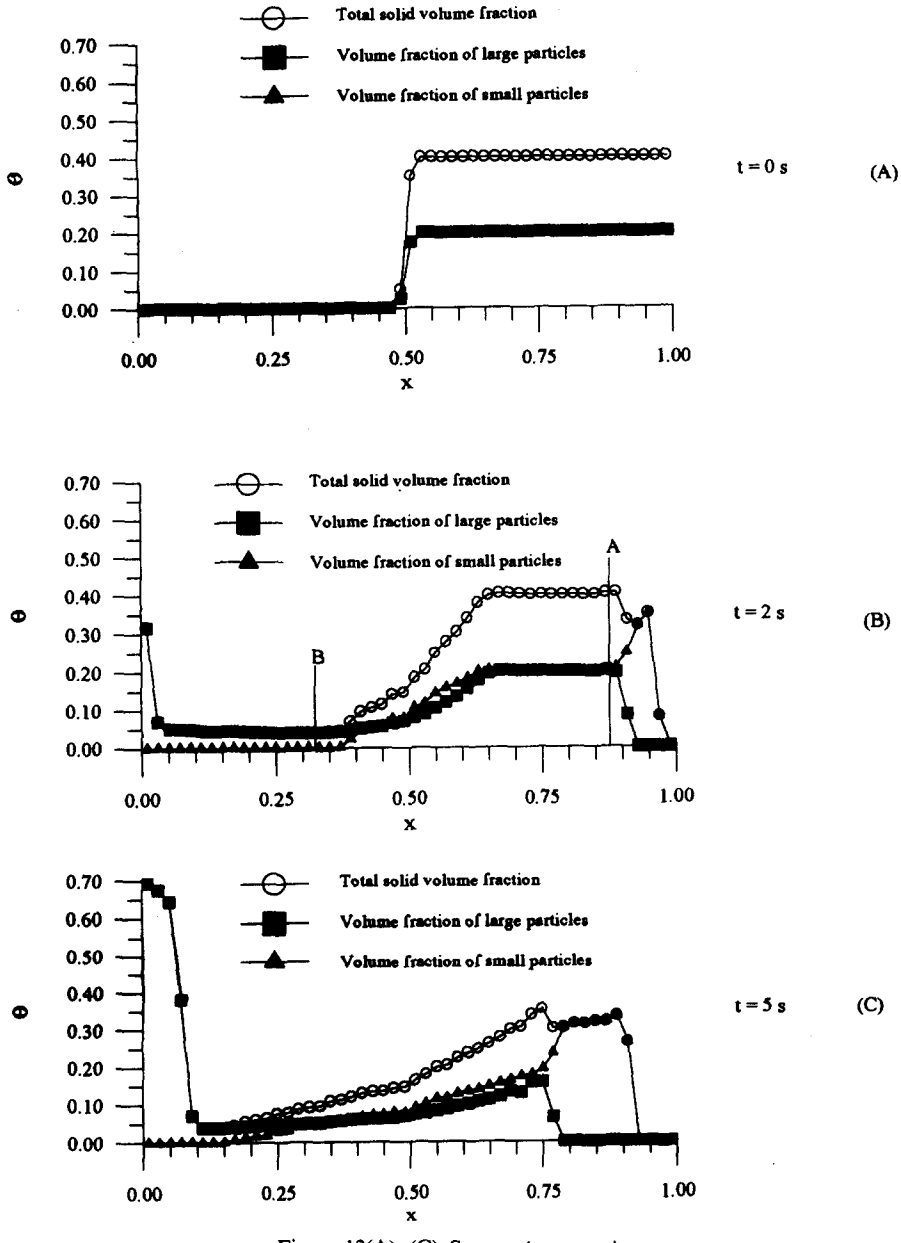

Figure 12(A)–(C) *See caption opposite.*

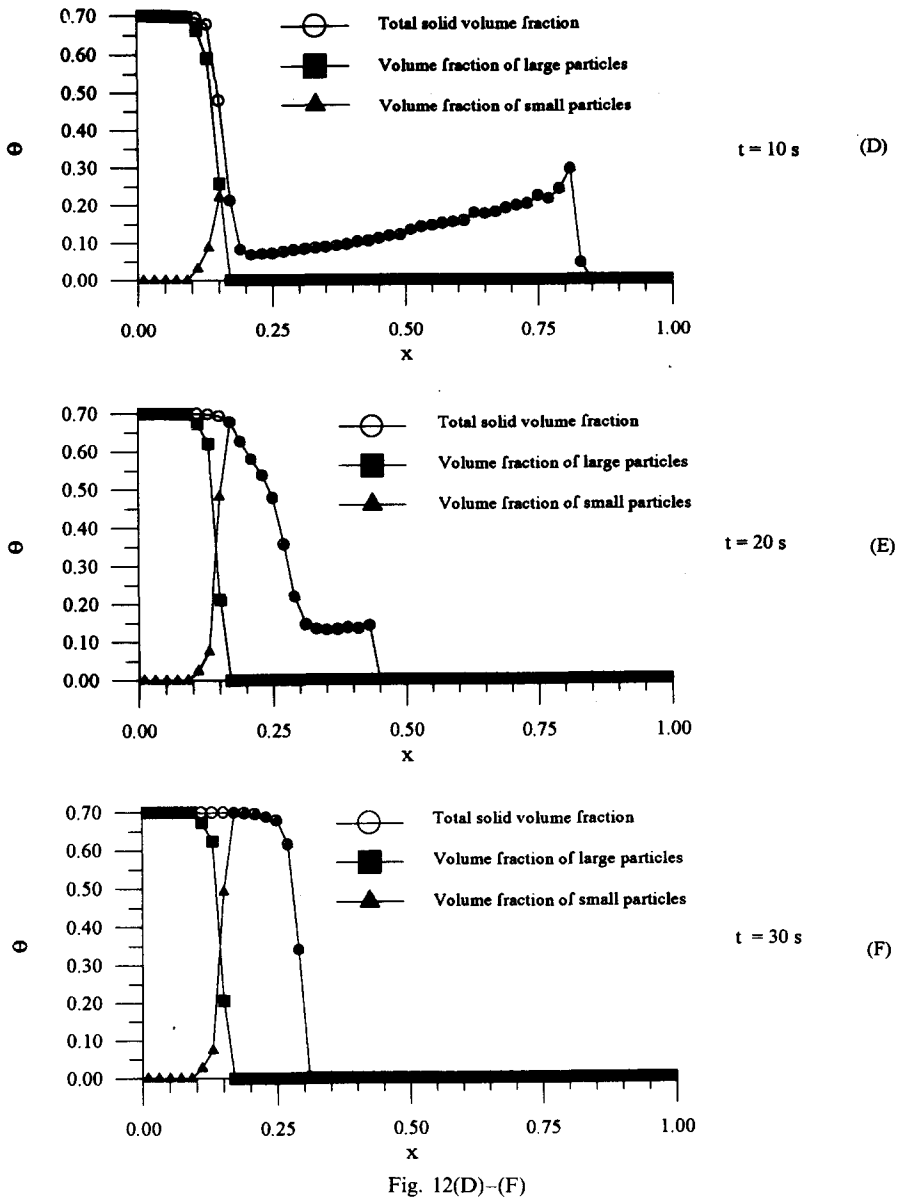

Fig. 12(D)-(F)

Figure 12. Particle volume fractions for the separation of a binary mixture.

Equation [54] reveals that we should expect point (C), where $\theta = 0$ in figure 9, to fall with a velocity of $-\Delta u$. However, at point (B) ($\theta_0 = 0.2$) the characteristics velocity is $0.13\,\Delta u_m$, so the mixture edge at (B) should rise at a velocity of 5.76×10^{-3} (s). The top edge of the mixture slug should fall at the solids velocity $-\epsilon_0 \Delta u_m$.

So points (A) and (B) on figure 9 approach one another as the slug falls. The dependence of Δu_m between (B) and (C) on ϵ means the linear solution of the last problem does not apply. However, for small values of θ near (C) $\Delta u_m \simeq \Delta u_\infty$, and we should expect a linear profile. Since the profile rises at (B) but falls in the region of (C) we might expect to see a rounding of the corner at (B). The solids should compact once (C) reaches the bottom of the container. The highly non-linear nature of Δu_m prevents an analytical estimate of the increase in the depth of the compact region.

Figure 10 shows the computed solids volume fraction at 2 and 5 (s). Also marked on the plot are the analytical results for points (A), (B), and (C) at the two times indicated with subscripts 2

and 5. Excellent agreement is seen between computed and analytical results. The curvature at point (B) is clearly shown, as is the linear lower profile for values of θ up to 0.15.

Figure 10 also shows the computed solids volume fraction profile at 10, 20 and 30 (s). Most of the particles have settled to the bottom by 20 (s) and formed a sediment layer with a relatively sharp upper surface and with a volume fraction near the close packing limit. However, the figure shows that at 30 (s) the sediment bed has continued to compress and forms a very sharp interface. At this late time the bed supports its own weight, which would not be possible without the intergranular stress terms.

9. SEPARATION OF A BINARY MIXTURE

This problem extends the granular sedimentation problem by considering the separation of a homogeneous binary mixture particles with diameters 1 and 2 (mm). Figure 11 shows the initial volume fraction distribution. Table 6 gives other computational details.

Figure 12(a)–(f) shows computed volume fraction profiles at times of 0, 2, 5, 10, 20 and 30 (s). The initial volume fraction profiles are shown in figure 12(a). Figure 12(b) shows the volume fractions at 2 (s). The larger particles fall faster because they have a lower surface to volume ratio and hence reduced effect of drag. Consequently, the larger particles collect on the bottom. The small particles sediment more slowly, so that some are still left at the top. Figure 12(b) shows an interesting effect, where above the large particles at the top of the domain the volume fraction of the small particles has increased to a maximum of 0.35, which is well above their initial volume fraction of 0.2. This local compaction of small particles above large particles is caused by the faster fall of large particles that causes upward gas motion and also a net solids volume fraction that is lower than the initial one. The upward gas motion tends to lift small particles up from below. The reduction in solids volume fraction implies an increase in gas volume fraction and hence a decrease in C_d given in [6]. Thus, a reduction in C_d for the small particles at the top of the slug causes them to accelerate and form a local compaction above the binary mixture.

Before discussing figure 12(c)–(f), we note that there are characteristic solutions for the profiles in figure 12(b) similar to those of granular sedimentation problem. In particular, the lower edge of the large particle volume fraction profile in figure 12(b) is in free fall over the first 2 (s) with a velocity $v_{p,2} = \Delta u_{\infty,2} = G/D_{s,2}$, with a large particle Stokes time scale $D_{s,2}$ of 4/90, giving a velocity of 0.4 (m/s). Consequently by 2 (s) the large particles have reached the bottom where they are collecting. The lower edge of the small particle volume fraction falls at $v_{p,1} = \epsilon^{3.65}\,\Delta u_{\infty,1}$. Figure 12(b) shows $\epsilon = 0.94$ at the lower edge, giving the analytical result (B) shown on the figure. Similarly, the top edge of the mixture at C falls with a velocity $\epsilon^{3.65}\,\Delta u_{\infty,2}$ because the large particles fall faster. Both of these analytical results compare well with the computed profiles. The slight discrepancy is due to the finite time acceleration of the particle mixture to the drift flux solution. The transient development of the large particle volume fraction profile coupled with the non-linear dependence of drag on ϵ prevents the formulation of detailed analytical solutions.

Inspection of the computed volume fraction profiles at 5 (s) in figure 12(c) reveals that the large particles have just reached the close packing limit at the bottom of the domain and are beginning to compact. The total solids volume fraction is an even mixture of small and large particles, with a local compaction of small particles at the top of the mixture that is now wider than at 2 (s). Figure 12(d) shows that at 10 (s) the large particles have all fallen to the bottom of the container. Furthermore, the volume fraction profile of the small particles shows they are collecting on top

Table 7. Solid volume percentage for the batch settling problems

Particle grade	Grade 8	Grade 10	Grade 12	
(Davies 1968)	$\begin{pmatrix} d_{mean} = 500\ \mu m \\ d_{min} = 420\ \mu m \end{pmatrix}$	$\begin{pmatrix} d_{mean} = 300\ \mu m \\ d_{min} = 220\ \mu m \end{pmatrix}$	$\begin{pmatrix} d_{mean} = 170\ \mu m \\ d_{min} = 110\ \mu m \end{pmatrix}$	Total
Case A	10%	9%	6%	25%
Case B	20%	9%	6%	35%
Case C	20%	9%	12%	41%
Case D	20%	17%	12%	49%

of the large particles. At 20 (s) the large particle volume fraction profile shows a compacted region at the bottom, with a slightly diffuse mixture interface of the two particle sizes. The small particles continue to collect on top of the large ones. By 30 (s) the mixture has separated out with large particles on the bottom and small particles resting on top. The volume fraction profiles are close to the prescribed maximum packing limit of 0.7 and are stationary.

10. BATCH SETTLING OF A TERTIARY PARTICLE MIXTURE

In this last problem, taken from Davies (1968), we consider the batch settling of a homogeneous mixture of three particle sizes. The suspending fluid is kerosene at 25°C ($\rho = 800\,\text{kg/m}^3$, $\mu = 1.9 \times 10^{-3}\,\text{Ns/m}^2$), and the solid phase is glass ($\rho = 2.93 \times 10^3\,\text{kg/m}^3$). Davies reported a narrow size distribution around a mean for each of the three different particle sizes. The mean particle diameters were 500, 300 and 170 μm. The relatively large particle sizes and low viscosity fluid result in maximum particle Reynolds numbers of about 5.

As a consequence of the Reynolds numbers, the second term in the drag law [6], is expected to be significant; and the hindered settling analytical methods of Lockett & Al-Habbooby (1973) and Mirza & Richardson (1979) are perhaps inaccurate. We note that Davies measured the interface velocities of separating particle sizes by observing colors associated with each particle size distribution. Hence, the last particle in a particle distribution determines the position of the interface, and this last particle corresponds to the smallest particle in the distribution.

The mean and smallest sizes for each distribution are summarized in table 7, and measurements for the four volume fraction cases of Davies (1968) are given in figure 13. The MP-PIC method is well-suited to handle the particle size distribution given by Davies, but in our computation we have taken a homogeneous mixture of each particle size, using the smallest size for each distribution and the associated size volume fraction of table 7. The volume fraction variation due to differential particle velocities is expected to be a secondary effect because the particle size distributions are relatively narrow and because no individual distribution volume fraction dominates the total. Our use of discrete particle sizes means that this problem is also well suited as a test problem for a four-fluid algorithm, one fluid for the kerosene, and one each for the three particle sizes, and also may be computed with the method of Mirza & Richardson (1979).

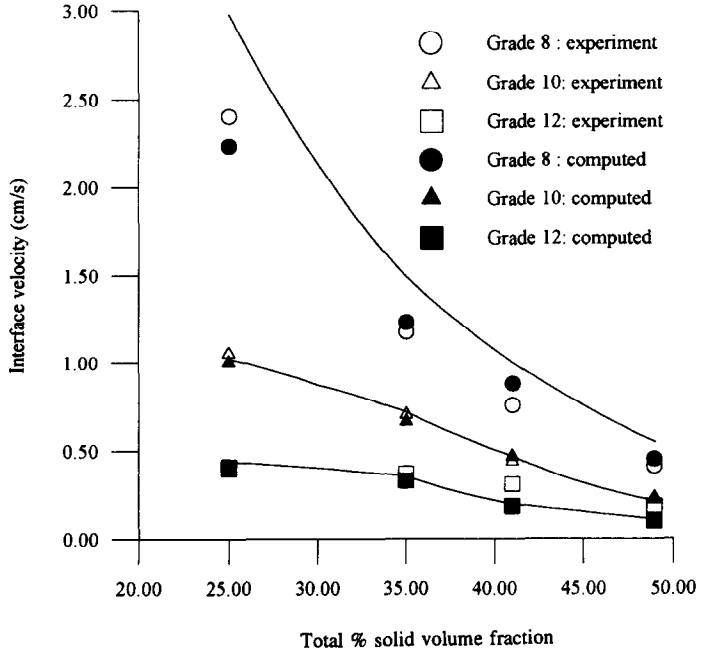

Figure 13. Interface velocities for batch setting. Open symbols are experimental data from Davies (1968), solid symbols are computed results and the solid line is from the drift flux theory of Mirza & Richardson (1979).

Table 8. Computational details for batch settling, for case A

Small particle radius (μm)	55
Number of small particles per parcel	2.8698×10^8
Number of parcels with small particles	300
Medium particle radius (μm)	110
Number of medium particles per parcel	5.3809×10^7
Number of parcels with medium particles	300
Large particle radius (μm)	210
Number of large particles per parcel	8.5928×10^6
Number of parcels with large particles	300
Number of computational cells	100
Time step (s)	0.01
Length of computational domain (m)	1
Initial position of parcels	Uniform spacing between 0 and 1 m

Calculation details for case A of table 7 are summarized in table 8, details for cases B, C and D of table 7 are similar with appropriate adjustments to the number of particles per parcel to give the volume fractions of table 7. It is interesting to note that Davies reported significant interlocking of binary particle sizes for solid volume fractions above 40%, but that for tertiary mixtures three distinct boundaries were observed and no interlocking was observed up to 50%. This interlocking effect is not presently incorporated in our model but will be the object of future work. We also note that Lockett & Al-Habbooby (1973) report a measured hindered settling function, $f(\epsilon) = \epsilon^n$, with a value for n of approximately 5 for the particle sizes of Davies. This value corresponds to a value of -3 in the drag function of [6] rather than the -2.65 previously used. We have modeled these problems with the constitutive equation [3], taking γ as 1.4 and a reference pressure of 1 atm. This corresponds to a sound speed in kerosene of 10 m/s, well above the particle and liquid velocities, giving a reasonable approximation of an incompressible fluid.

Figure 13 presents a comparison of the interface velocities measured by Davies and those obtained by measuring the volume fraction "shocks" computed from the MP-PIC method. Open symbols are experimental data, and closed symbols the corresponding computed values. The figure shows good agreement between experimental measurements and computations over the whole range of total solid volume fraction. Also included on the plot, shown as solid lines, are results of drift flux calculations using the method of Mirza & Richardson (1979). This calculation procedure is well known and tested for homogeneous batch sedimentation of low Reynolds number particles. Figure 13 shows that the drift flux calculation does poorly for the velocity of the lowest (fastest moving) interface. This is due to the relatively high particle Reynolds numbers ($Re_p \approx 5.0$). The interface velocities between the mid-size ($Re_p \approx 1.0$) and small particle zones, and the small particle ($Re_p \approx 0.2$) and clear kerosene, are predicted well by the drift flux solution. This is to be expected because the particle Reynolds numbers are small.

11. CONCLUSIONS

A new method for the simulation of multiphase particulate flows called MP-PIC has been described. The MP-PIC method extends the well-known PIC methods but differs significantly by allowing separate gas and particle velocities. The governing equations of multiphase flow are derived for use with our MP-PIC method using a Boltzman approach and then closely related to a Eulerian continuum description. These closely coupled formulations allowed us to take the best of Eulerian and Lagrangian methods and produce a formulation that can readily handle a distribution of particle characteristics.

Six test problems have been described and then solved with the MP-PIC method. The test problems have shown that the method can accurately compute the speed of sound in a particulate mixture and the speed of a stress wave. A calculation for the fall of a dispersed particle slug revealed that the MP-PIC method has negligible numerical diffusion in the calculation of particle advection. An analytical solution for the problem was given and accurately computed. A calculation for the sedimentation of a granular mixture revealed that the MP-PIC method can simulate the whole sedimentation process including late time compaction to the close packing limit. The analytical solution was extended to this densely packed problem and showed the computed solutions were

accurate. A test problem for the separation of a binary mixture demonstrated the power of the MP-PIC method to handle different particle characteristics. This problem shows complex interactions that take place in a relatively simple separation problem, in particular the appearance of local compaction interfaces and the separation of small particles on top of large ones. The last problem compares our computational simulation with experimental data from Davies (1968) for batch settling of a tertiary particle mixture. Our results compared very well with all the experimental data. Of note is the agreement at high particle Reynolds numbers (~ 5) which was attributed to the $Re^{2/3}$ dependence in the drag function. These large particle Reynolds numbers, and tertiary mixture, make this a practically important problem.

These six one-dimensional test problems served to demonstrate the accuracy and power of the MP-PIC method.

Acknowledgements—Andrews acknowledges support from an AWU-DOE Faculty Fellowship to perform this research while at Los Alamos during the summer of 1994. O'Rourke's work was funded by Conservation and Renewable Energy, Advanced Industrial Concepts Division of the United States Department of Energy.

REFERENCES

Andrews, M. J. 1993 The large-scale fragmentation of the intact liquid core of a spray jet. *Atom. Sprays* **3,** 29–54.

Andrews, M. J. & Bracco, F. V. 1989 On the structure of turbulent dense spray jets. In *Encyclopedia of Fluid Mechanics* (Edited by Cheremisinoff, N. P.) Vol. 8, pp. 1063–1089. Gulf Publishing, Houston, TX.

Batchelor, G. K. 1988 A new theory of the instability of a uniform fluidized bed. *J. Fluid Mech.* **193,** 75–110.

Davies, R. 1968–1969 The experimental study of the differential settling of particles in suspension at high concentrations. *Power Technol.* **2,** 43–51.

Gidaspow, D. 1986 Hydrodynamics of fluidization and heat transfer: supercomputer modeling. *Appl. Mech. Rev.* **39,** 1–22.

Gidaspow, D. 1994 *Multiphase Flow and Fluidization Continuum and Kinetic Theory Descriptions.* Academic Press, Boston, MA.

Gidaspow, D., Bahary, M. & Jayaswal, U. K. 1994 Hydrodynamic models for gas–liquid–solid fluidization. *Numerical Methods in Multiphase Flows,* FED-Vol. 185. ASME, New York.

Harlow, F. H. 1964 The particle-in-cell computing method of fluid dynamics. In *Fundamental Methods in Hydrodynamics* (Edited by Alder, B., Fembach, S. & Rotenberg, M.). Academic Press, New York.

Harris, S. E. & Crighton, D. G. 1994 Solitons, solitary waves, and voidage disturbances in gas-fluidized beds. *J. Fluid Mech.* **266,** 243–276.

Kuo, K. K. 1986 *Principles of Combustion.* Wiley, New York.

Kynch, G. J. 1952 Theory of sedimentation. *Trans. Faraday Soc.* **48,** 166–176.

Lockett, M. J. & Al-Habbooby, H. M. 1973 Differential settling by size of two particle species in a liquid. *Trans. Inst. Chem. Engrs* **51,** 281–292.

Lyczkowski, R. W., Gidaspow, D. & Solbrig, C. W. 1978 Characteristics and stability analysis of transient one-dimensional two-phase flow equations and their finite difference approximations. *Nucl. Sci. Engng* **66,** 378–396.

Mirza, S. & Richardson, J. F. 1979 Sedimentation of suspensions of particles of two or more sizes. *Chem. Engng Sci.* **34,** 447–454.

O'Rourke, P. J. 1981 Collective drop effects on vaporizing liquid sprays. Ph.D. thesis, Princeton University, NJ.

O'Rourke, P. J. 1985 The acoustic mode in numerical calculation of subsonic combustion. In *Combustion and Nonlinear Phenomena* (Edited by Clavin, P. C., Larrouturou, B. & Pelce, P.). Les Edition de Physique, Paris.

O'Rourke, P. J. 1989 Statistical properties and numerical implementation of a model for droplet dispersion in a turbulent gas. *J. Computational Phys.* **83,** 345–360.

O'Rourke, P. J., Brackbill, J. U. & Larrouturou, B. 1993 On particle-grid interpolation and calculating chemistry in particle-in-cell methods. *J. Computational Phys.* **109,** 37–52.
Putnam, A. 1961 Integratable form of droplet drag coefficient. *J. Am. Rocket Soc.* **31,** 1467–1468.
Richardson, J. F. & Zaki, W. N. 1954 Sedimentation and fluidization: part I. *Trans. Inst. Chem. Engrs* **32,** 35–53.
Rizk, M. A. 1993 Mathematical modeling of densely loaded, particle-laden turbulent flows. *Atom. Sprays* **3,** 1–27.
Travis, J., Harlow, F. & Amsden, A. 1976 Numerical calculation of two-phase flows. *Nucl. Sci. Engr.* **61,** 1–10.
Wallis, G. B. 1969 *One-dimensional Two-phase Flow.* McGraw–Hill, New York.
Williams, F. A. 1985 *Combustion Theory*, 2nd Edn. Benjamin/Cummings, Menlo Park, CA.

APPENDIX A

Evaluation of Numerical Coefficients

The following are the explicitly known coefficients of [36] and [42] of this paper:

$$A_{i+1/2} = \frac{1}{\Delta x(\rho_G \epsilon)^n_{i+1/2}} \sum_{\mathrm{p}} \left[N_{\mathrm{p}} m_{\mathrm{p}} T_{i+1/2}(\tilde{x}_{\mathrm{p}}) \frac{D^n_{\mathrm{p}}}{1+\Delta t D^n_{\mathrm{p}}} \right] \quad [A1]$$

$$B_{i+1/2} = \frac{1}{\Delta x} \sum_{\mathrm{p}} \left[N_{\mathrm{p}} m_{\mathrm{p}} T_{i+1/2}(\tilde{x}_{\mathrm{p}}) \frac{D^n_{\mathrm{p}}(v^n_{\mathrm{p}} - \Delta t g)}{1+\Delta t D^n_{\mathrm{p}}} \right] \quad [A2]$$

$$C_{i+1/2} = \frac{1}{\Delta x} \sum_{\mathrm{p}} \left[N_{\mathrm{p}} \frac{m_{\mathrm{p}}}{\rho_{\mathrm{s}}} T_{i+1/2}(\tilde{x}_{\mathrm{p}}) \frac{1}{1+\Delta t D^n_{\mathrm{p}}} \right] \quad [A3]$$

$$D_{i+1/2} = \frac{1}{\Delta x \tilde{\theta}_{i+1/2}} \sum_{\mathrm{p}} \left[N_{\mathrm{p}} \frac{m_{\mathrm{p}}}{\rho_{\mathrm{s}}} T_{i+1/2}(\tilde{x}_{\mathrm{p}}) \frac{\Delta t D^n_{\mathrm{p}}}{1+\Delta t D^n_{\mathrm{p}}} \right] \quad [A4]$$

$$E_{i+1/2} = \frac{1}{\tilde{\theta}_{i+1/2} \Delta x} \sum_{\mathrm{p}} \left[N_{\mathrm{p}} \frac{m_{\mathrm{p}}}{\rho_{\mathrm{s}}} T_{i+1/2}(\tilde{x}_{\mathrm{p}}) \frac{1}{1+\Delta t D^n_{\mathrm{p}}} \right] \quad [A5]$$

$$F_{i+1/2} = \frac{1}{\Delta x} \sum_{\mathrm{p}} \left[N_{\mathrm{p}} m_{\mathrm{p}} T_{i+1/2}(\tilde{x}_{\mathrm{p}}) \frac{D^n_{\mathrm{p}} v^n_{\mathrm{p}} + g}{1+\Delta t D^n_{\mathrm{p}}} \right]. \quad [A6]$$